Anomalous Boundary Behavior in Non-Newtonian Fluids at Amphiphobic Surfaces

Xingwei Wang,[1,2] Luyao Bao,[1] Jun Wen,[3] Daniele Dini,[3] Jianbin Zhang,[1] Li Sun[1] Wufang Yang,*[,1,4] Feng Zhou,*[,1,4] Weimin Liu*[,1,2]

[1] State Key Laboratory of Solid Lubrication, Lanzhou Institute of Chemical Physics, Chinese Academy of Sciences, Lanzhou, Gansu Province, China.

[2] School of Materials Science and Engineering, Northwestern Polytechnical University, Xi'an, Shannxi Province, China.

[3]Tribology Group, Department of Mechanical Engineering, Imperial College London, South Kensington Campus, Exhibition Road, London, SW7 2AZ, UK.

[4]Yantai Zhongke Research Institute of Advanced Materials and Green Chemical Engineering， Yantai 264006, China

ABSTRACT

In this work, the effect of amphiphobic surfaces on the rheological behavior and boundary slip of the shear thickening fluids (STFs) was investigated. The experimental results suggested the viscosities were diminished, shear thickening was delayed and weakened, and an ultrahigh drag reduction was obtained. Furthermore, slip length was observed to vary with shear rate. Dissipative particle dynamics (DPD) simulations were adopted to further investigate these specific rheology and slip behavior. The simulation results conformed with experiments and established a linear relationship between the slip length and viscosity. We consider this study could be a conducive practical reference for the investigation of boundary slip in complex fluids and possibly a crucial protocol for analyzing STFs' manipulation.

KEY WORDS: shear thickening fluid; boundary slip; drag reduction; slip length; amphiphobic surface

1. INTRODUCTION

Among all the known properties of a solid-liquid interface, wettability comes across as the most instrumental characteristic governing the adhesive and cohesive interactions between a solid and a liquid. Regulation of the surface wettability tends to influence several vital aspects, such as heat transfer[1], adhesion[2] and skin friction drag[3] of liquid-to-solid and liquid manipulation[4]. Taking liquid super-repellent surfaces as an example, liquid droplets interacting with such surfaces are characterized by a static contact angle (CA) approaching 180° and a contact-angle hysteresis (CAH) near 0°; that is, its adhesion and friction with liquid is ultralow, which endorses multiple practical applications in fields of self-cleaning[5], corrosion prevention[6], drag reduction[7] and liquid separation[8]. Currently, the thriving contemporary industrialization has rendered the practice of fluid transportation through pipelines both prevalent and indispensable. Consequently, the topic of skin friction drag between pipelines and fluids seems to have drawn immense attention owing to the critical impact on the energy efficiency conservation as well as the maintenance of such equipment. Additionally, the development of advanced micro-fluidic devices with the advantages of all-in-one chip further necessitates an inclusive insight into the regulation of the interaction between fluids and solids. For this reason, minimizing the resistance by varying the degree of wetting at the liquid-solid interface is a common quest naturally pursued by the majority of researchers. Many numerical simulation, theoretical calculations and experimental research efforts have been conducted in the perspective of manipulating wettability to minimize friction drag.[9-14] At present, a large amount of experimental and theoretical studies have supported a rather assertive description: On the non-wettable surface, the no-slip boundary condition for the liquid-solid turns into a slip boundary condition due to the substantial softening of the solid-liquid interactions carried out by the chemical composition and morphology of surfaces. When a liquid flows over such surfaces, a slip velocity is generated that corresponds to

a constant slip length typically spanning in the nanometer to micrometer range.[15-18] This constant slip length has nothing to do with flow velocity, only determined by the interface.[13, 19-20]

Although extensive researches have been conducted focusing on boundary slip, the majority of these studies were predominantly carried out using Newtonian fluids. At present, boundary slip of non-Newtonian fluids is far from being fully understood; our investigation has as its main task to explore this using a combined experimental and modelling approach. Shear thickening fluids (STFs) as one kind of typical non-Newtonian fluid have been widely studied in the field of soft-body armor, shock absorption, damping and energy utilization because of the order-of-magnitude increment in viscosity under high shear.[21-23]. For example, the STFs treated Kevlar fabrics composites could act as novel bullet-proof materials to defend soldiers and combat equipment. [24] However, the same increase in viscosity can result in jamming and failure of pumping and mixing equipment utilizing STFs. [25] As a result, the shear thickening attribute needs to be sidestepped at times to avoid damage. However, the ability to tune the STFs viscosity remains challenging. Currently, the passive measure adopted to tune shear thickening viscosity tends to alter the physical properties of suspension constituents, such as volume fraction [26-27], particle roughness [28-29], particle surface chemistry [21], and solvent attributes [30-31]. Though these methods can affect the shear-thickening behavior of STFs, they cannot be regulated in real-time according to specific conditions. This could however be achieved by tuning the friction interaction between STFs and the wall surface using super-repellent surfaces, which can support slip boundary conditions and reduce the shear to STF, thereby dramatically delaying or diminishing its shear thickening propensity and modulate its response.

For this study, STFs are meaningfully selected to investigate the interaction between non-Newtonian fluid and surfaces with different wettability, and to unravel the effect generated by the use of amphiphobic surfaces on the slip behavior and rheological properties of STFs. The experiments and simulation suggested that under the slip boundary condition, an ultrahigh drag reduction (DR) was obtained and the viscosity

of STF was drastically reduced, followed by the delaying of the shear thickening transition, indicating that the interaction between STFs and substrate had decreased considerably. More importantly, a specific slip phenomenon characterized by the slip length first decreasing and subsequently increasing with shear rate was observed; afterwards, dissipative particle dynamic (DPD) simulation was adopted to demonstrate this abnormal slip phenomenon, which established a linear relationship between the slip length and the viscosity. This research has shed light on the relationship between the behavior of complex fluids under shear and non-repellent surfaces, providing much insight to be able to broaden and better control the application of STFs to a number of areas, including petrochemical industry, microfluidics, transportation…

2. EXPERIMENTAL DETAILS

2.1. Materials and Chemicals

Aluminum sheet (99.99%) is purchased from Grikin Advanced Materials Co. Ltd. Ammonium hydroxide ($NH_3 \cdot H_2O$, 28%), anhydrous ethanol and polyethylene glycol (PEG-400) were purchased from Shanghai Chemical Reagent Co. Ltd. Tetraethyl orthosilicate (TEOS, 98%) and1H,1H,2H,2H-perfluorooctyltrichlorosilane (PFOTS, 97%) were purchased from Sigma-Aldrich. Deionized water with a resistivity of 18.2 MΩ/cm was produced by a Milli-Q water purification system.

2.2. Preparation of SiO_2 nano-particles and shear thickening fluids (STFs)

As depicted in **Figure S1**, silica nanoparticles (NPs) with 240 nm diameter were prepared according to the most suitable methodology outlined in the literature. [32-33] The typical experimental process is as follows: ammonium hydroxide (10.0 mL)， anhydrous ethanol (30.0 mL) and distilled water (6.0 mL) were added into a beaker, then TEOS (2.0 mL) was added into the beaker dropwise under stirring. The silica NPs were fabricated via the sol-gel reaction at room temperature for 2.5h. The obtained silica NPs were collected by high-speed centrifugation and washed with distilled water and ethanol repeatedly. Finally, the NPs were dried under vacuum overnight. Shear

thickening fluids were prepared by ultrasonic dispersing silica NPs into PEG-400.

2.3. Preparation of the amphiphobic Al_2O_3 substrate

The preparation of amphiphobic anodized alumina was carried out according to the electrochemical etching method.[34] In constant voltage mode (4 V bias), the ultrasonically cleaned Al sheet was etched in 10 g/L NaCl solution at room temperature for 3 h. And then, the etched Al sheet was anodized at a current density of 0.325 A/cm^2 to form nanostructures. **Figure S2** is the FE-SEM images of the etched aluminum plate with a micro-nano composite structure. In order to obtain a desired amphiphobic property, a PFOTS self-assembled monolayer was applied to modify the surface chemistry of etched aluminum sheets through a liquid deposition method.

2.4. Characterization

Micromorphology images were obtained using a field emission scanning electronic microscope (FE-SEM, JSM-6701F) at 5−10 kV. Transmission electron microscopy (TEM) images were obtained using a TECNAI G2 TF20 (FEI, USA). The adhesive force was measured by a high-sensitivity micro-electromechanical balance system (Data physics TCAT 11, Germany). 5 μL STF droplet was hanged on an oleophilic metal ring. A micro-balance detector was connected to the ring to record instantaneous adhesive force during the test. The amphiphobic surface was placed on a movable stage, and this retractable stage could drive the substrate upwards or downwards at a constant speed. The stage firstly moved upward until the amphiphobic substrate contacted sufficiently with the suspended STF droplet, then it started to move away from the droplet surface. The adhesive force was digitally recorded and was shown to raise first and then decrease after reaching the maximum during the testing process. The peak data recorded in the force-distance curve was taken as the breakpoint adhesive force. The effect of varying boundary conditions on the rheological behaviors of STFs and their corresponding boundary slip were characterized through a rheometer (HAAKE, RS6000, Germany) in Couette flow. For the rheological experiments, constant rate

mode and plate-and-plate arrangement mode were applied, in which the STFs fluid is confined between two parallel plates and can flow under a given shear rate. The diameter of these plates is 35 mm and their spacing is 1 mm. In this configuration, the valid shear rate spans the range from 0.001 s^{-1} to 1500 s^{-1} and shear stress spans the range from 0.001 Pa to 10000 Pa, which can completely cover the range of measurement. The shear viscosity and shear stress can be recorded simultaneously. In order to ensure that a complete rheological behavior can be observed, including shear thinning and shear thickening, reasonable shear rate ranges were predetermined for STFs with different volume fractions.

3. RESULTS AND DISCUSSION

As shown in **Figure 1**, the system in which STFs flow over the amphiphilic stainless-steel surface was considered as corresponding to a no-slip boundary condition. In this case the boundary slip velocity at solid-liquid interface was zero. However, the slip boundary condition was induced when the plates were replaced with amphiphobic substrates; the condition in which the lower plate is replaced by an amphiphobic substrate is regarded as a “one-slip” condition, whereas the condition in which both the upper and lower plates are replaced by amphiphobic substrate is regarded as a “two-slip” condition.

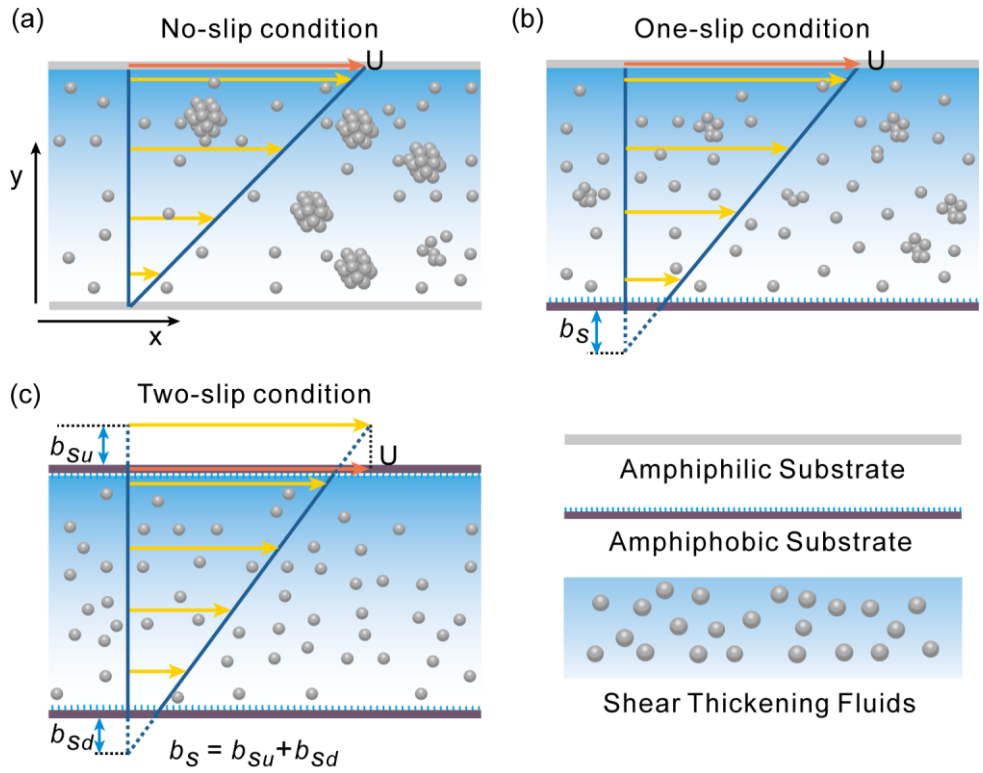

Figure 1. Schematic illustration of the Couette flows of STFs with no-slip and slip boundary conditions and the definition of slip lengths b_s.

The dependence of STFs rheological properties on NPs content are firstly studied and the rheological curves for STFs with increasing NPs volume fraction are shown in **Figure 2**. At low but increasing shear rate, the shear thinning phenomenon is obviously observed, which is associated with formation of particle layers[35-36]. However, once the critical shear rate ($\dot{\gamma}_c$, above which the shear viscosity increases sharply) is reached, the shear viscosity rises exponentially and increases up to the maximum shear rate ($\dot{\gamma}_{max}$, where the shear thickening transition is complete). As has been reported previously, shear thickening is induced by the formation of clusters with the combined action of both hydrodynamic force and frictional contact among NPs [21, 37-38]. On the other hand, the initial shear viscosity, critical shear rate and maximum shear rate are also dependent on the volume fraction of NPs, and the initial shear viscosity increases with increasing the volume fraction of NPs, while the $\dot{\gamma}_c$ and $\dot{\gamma}_{max}$ decrease with the increase of NPs content. As a consequence, STFs with a varying volume fraction of NPs were prepared to investigate the effect of different boundary conditions on rheological

behaviors and boundary slips of non-Newtonian fluids.

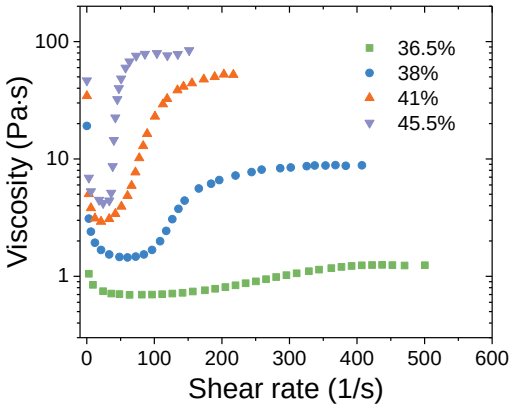

Figure 2. Viscosity curves as functions of shear rate for STFs with increasing NPs volume fractions.

To study the rheology of these fluids under different boundary conditions, the viscosities and shear stress were measured as functions of shear rate for STFs with various NPs volume fractions under no-slip and slip conditions (**Figure 3**). Compared with no-slip condition, the observed shear stress and viscosities for both one-slip condition and two-slip conditions are smaller under the same shear rate, indicating much weaker friction interaction between slip plate and STFs. Furthermore, the critical shear rates, $\dot{\gamma}_c$, corresponding to different boundary conditions are no longer identical. Their numerical values are summarized in **Table 1**. As shown in **Table 1**, critical shear rates vary not only as a function of the boundary conditions but also depend on the volume fraction of NPs in STFs. Regardless of the volume fraction of NPs, the $\dot{\gamma}_c$ increases as follows: no-slip condition, one-slip condition, and two-slip condition. Besides, the $\dot{\gamma}_c$ decreases with the increase of volume fraction of NPs even under slip boundary conditions. Concomitantly, compared with one-slip condition, the critical shear rate hysteresis (the difference between the critical shear rates for slip condition and no-slip one.) under two-slip condition is larger. This obvious increase of critical shear rate indicates that the interaction of STFs and substrate reduces by introducing slip boundary conditions. Therefore, reduced frictional resistance can be expected when

non-Newtonian fluid flows over amphiphobic substrate. Moreover, considering that the strength of the interaction between the substrate and the liquid flowing over it is another significant element to regulate liquid slip on solid surface,[11, 39-40] adhesion between STFs and amphiphobic/amphiphilic surfaces were measured as well. The quantified adhesion values of STF droplets with NPs volume fraction ranging from 33% to 45.5% are shown in **Figure S3**. Compared with the adhesion of STFs on a lyophilic stainless-steel substrate, lower adhesion is observed on lyophobic substrate. Furthermore, adhesion decreases with increasing the NPs volume fraction. These experimental results further substantiate that drag reduction effect can be expected for STFs flowing over the amphiphobic surface. Therefore, theDR is calculated using formula: $DR = \frac{\tau_{no-slip} - \tau_{slip}}{\tau_{no-slip}}$, where $\tau_{no-slip}$ and τ_{slip} are shear stress under no-slip and slip boundary conditions at the same shear rate. As shown in **Figure 3**, ultrahigh drag reductions are acquired. It can be seen that a maximum DR appears in the range of the onset to the end of shear thickening, whose location specifically depends on the speed of shear thickening. For STF with a 36.5% NPs volume fraction, the peak DR appears at the end of shear thickening under no-slip boundary, while for STF with a 45.5% NPs volume fraction, the maximum DR appears almost at the onset of shear thickening due to the different shear thickening continuities. As whole, it is notable that the peak DR is associated with a delayed and reduced shear thickening effect.

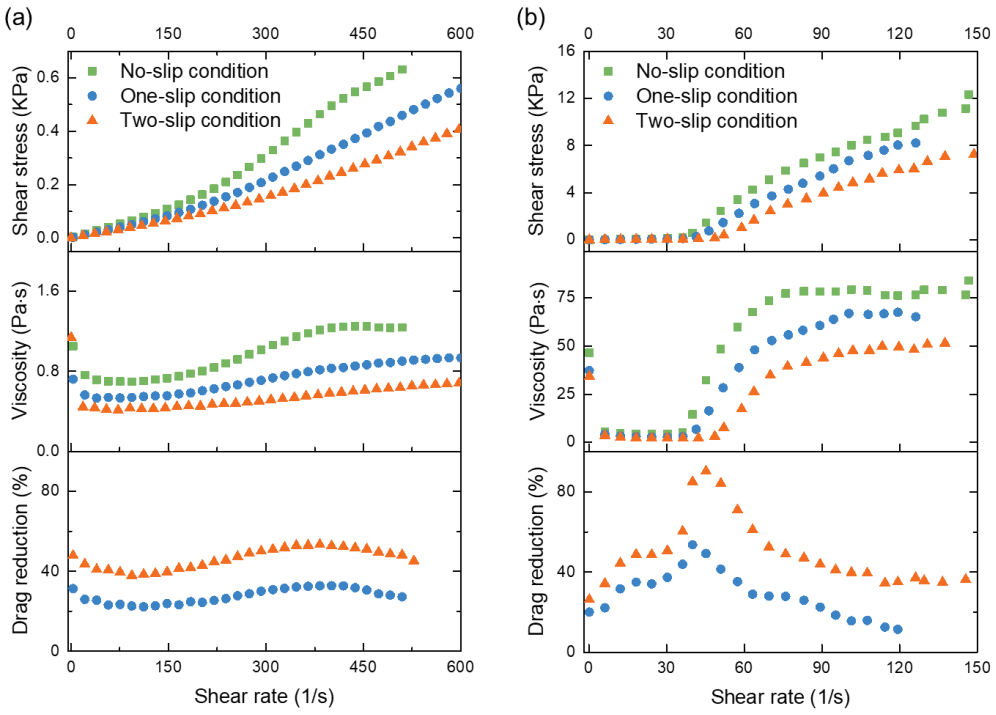

Figure 3. Flow curves and viscosity curves of STFs with NPs volume fraction being (a) 36.5% and (b) 45.5% under no-slip and slip boundary conditions and their corresponding drag reductions.

Table 1. Critical shear rates of STFs with different NPs volume fractions under distinct boundary conditions and their corresponding critical shear rate hysteresis.

Mass fraction	$\dot{\gamma}_c$/s^{-1}			$\Delta\dot{\gamma}_c$/s^{-1}	
	No-slip condition	One-slip condition	Two-slip condition	One-slip condition	Two-slip condition
45.5%	36.9	40.8	51.3	3.9	14.4
36.5%	160.8	172.3	195.4	11.5	34.6

The values obtained experimentally enable a quantitative estimate of the slip length. Because the viscosity of STFs varies with shear rate, the traditional way of determining slip length is no longer applicable here. Therefore, on the basis of the monotonic increasing character of the stress-rate curves of STFs, to determine the slip length of STFs, we assume that, under the same shear stress, they are subjected to the same shear

rate, which is defined here as the real shear rate ($\dot{\gamma}_{real}$). Due to the presence of slip velocity at the wall, the effective shear rate for the test with slip boundary conditions is not the real shear rate which each fluid experiences. So, we determine the shear rate applied by the rheometer to the fluid as apparent shear rate ($\dot{\gamma}_{app}$). For the test with no slip boundary condition, $\dot{\gamma}_{real}$ equals $\dot{\gamma}_{app}$. While for the test with slip boundary they differ, as illustrated in **Figure 4**.

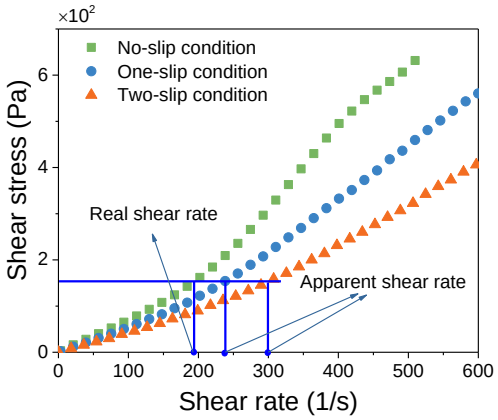

Figure 4. Two kinds of shear rate illustrated on the flow curves of STFs.

As shown in **Figure 4**, the slip length can be calculated using the following method: as it has been assumed that for fluids experiencing the same shear stress in the shear thickening regime, they are under the same $\dot{\gamma}_{real}$, the difference between $\dot{\gamma}_{app}$ for the tests with slip boundary conditions and $\dot{\gamma}_{real}$ for the test with no-slip boundary condition is caused by the boundary slip. Thus, the slip length can be simply estimated as $b_s = \left(\frac{\dot{\gamma}_{app}-\dot{\gamma}_{real}}{\dot{\gamma}_{real}}\right) \times h$, where b_s is the slip length at the wall surface, h is the shear height (the distance between the two shearing plates). It should also be noted here that the slip length for the two-slip condition tests is the sums of the slip lengths on both walls, and the two lengths are here assumed to be identical for simplicity.

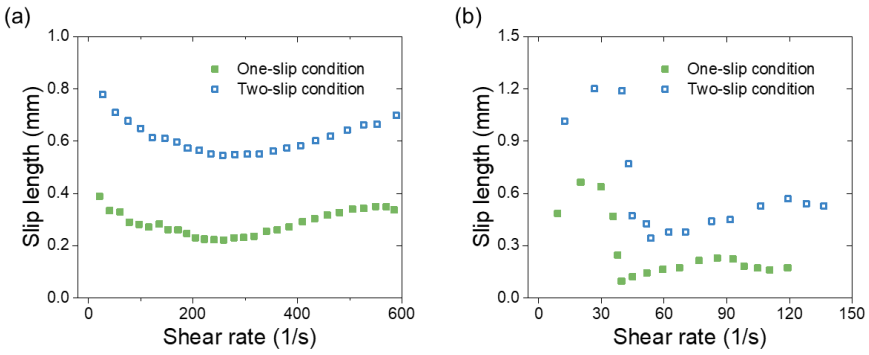

Figure 5. The total slip length as a function of shear rate for STFs with NPs volume fractions being (a) 36.5% and (b) 45.5%, respectively.

The slip length was calculated and plotted as a function of the apparent shear rate in **Figure 5**. From **Figure 5**, it is obvious to observe that the slip length first decreases and then increases with the apparent shear rate. The slip length decreases in the range of shear thinning and onset of shear thickening, subsequently increases in later range of shear thickening and even becomes somewhat constant after shear thickening in detail. This variation is more complex with the larger volume fraction of NPs, and surprisingly does not conform to the generally accepted constant slip length slip-model. It is expected that this is due to the non-Newtonian character of STFs. For the conventional constant slip length model, its premise is that the viscosity of the fluid is constant; this is not the case for STFs, whose viscosity varies with shear rate. As a result, we think the varying slip length is associated with the non-constant viscosity.

To further demonstrate the mechanisms responsible for this non-constant slip length for STFs, a numerical simulation based on dissipative particle dynamics (DPD) usually used for rough composite colloids simulation is adopted to model the non-Newtonian behavior of STFs [41] under no-slip and slip boundary conditions[42]; For further details of DPD approach, the readers should refer to the supporting information. **Figure 6** presents the shear stress (τ) and the relative viscosity (η_r) of the model STF at different Peclet numbers, $\mathrm{Pe} = 6\pi\eta_0\dot{\gamma}a^2/(k_BT/a)$ (, which represents the relative magnitude of shear forces to Brownian forces.), under different boundary conditions, where η_0 is the viscosity of the suspending fluid, a is the radius of the particle

(representing the NPs), k_B is Boltzmann constant and T is the absolute temperature. With the increasing of Pe, the system exhibits shear thinning followed by a shear thickening regime under both slip and no-slip boundary conditions. More importantly, the slip boundary condition reduces the shear stress and the viscosity of the system under the same applied shear rate. Furthermore, the Pe of the onset of shear thickening regime increases when slip boundary condition is considered, where this transition is detected for Pe ≈ 1.08 and Pe ≈ 2.31 for no-slip and slip boundary, respectively. As a result, a high DR is acquired, whose peak reaches 63% located at the end of shear thickening under no-slip boundary. These are consistent with the experimental results, indicating that the DPD simulations can successfully reproduce the changes in the system response due to the changes at the fluid/wall boundary.

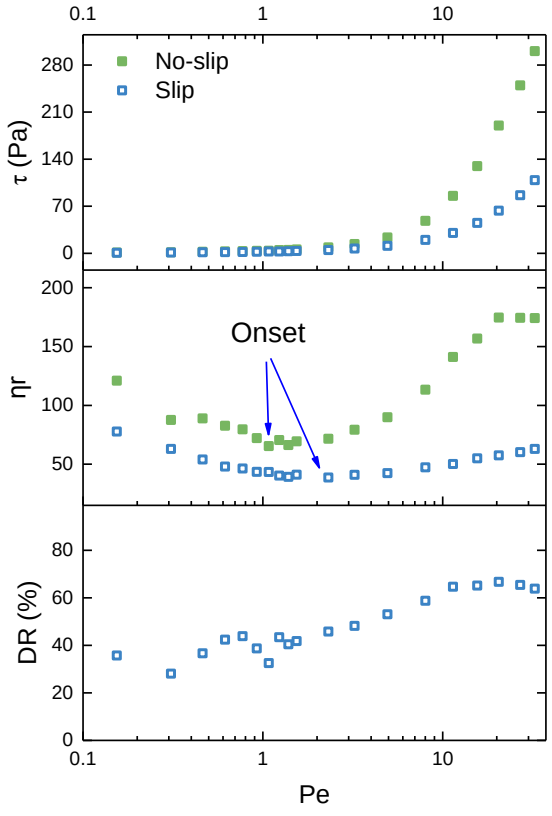

Figure 6. The rheology of model STFs under slip and no-slip boundary conditions and its corresponding drag reduction.

The detailed slip behavior of the system at different Pe numbers are extracted explicitly from the velocity profiles in the simulations. **Figure 7a** presents the velocity

profiles at different Pe numbers, which shows that the partial slip boundary condition appears at all Pe numbers. In **Figure 7a**, the two gray districts named as virtual boundary are mathematically defined to achieve the slip boundary condition during the simulation, whose specific implementation process can refer to the supporting information. The gradient of velocity profile is linearly fitted using the middlemost 12 velocities for each Pe number, and the fitted parameters are listed in **Table S1**. For the lowest two Pe numbers, the R-Squares are 0.07 and 0.89 due to the ultralow shear rate leading to very large statistical errors associated with the system noise (referencing **Table S1**). Except these two points, the R-Squares are always larger than 0.95. According to the definition of Navier slip boundary condition, the slip length is calculated and showed in **Figure 7b** with green squares. It can be seen that the slip length with increasing Pe numbers exhibits two regimes, i.e., the slip length decreases and increases with increasing Pe numbers in the first and second regimes, respectively. The transition between the two regimes occurs at Pe~O(2.31), which agrees well with the viscosity-Pe relationship. Before the transition, it belongs to shear thinning range where viscosity decreases, and after the transition, it belongs to shear thickening range in which viscosity increases. Furthermore, the slip length as a function of viscosity is shown in **Figure 7c**. It can be seen that the slip length and viscosity possess a linear relationship, which has been observed and reported by previous works such as L. Guo et al.[43], indicating that the non-constant slip length is caused by the change in viscosity. In additional, the slip length calculated according to the hypothesis that a shear stress corresponds to a single real shear rate is also presented in **Figure 7b**, marked with open blue square. It can be seen that the two slip lengths calculated with the two different methods have similar change trend roughly. In the range where the fluids exhibit shear thickening behavior slip lengths agrees better, but in shear thinning range, they coincide worse. We think the reason of deviation between these two kinds of variations calculated by different method is that the part values of shear rate are not accurate adequately because they are interpolated linearly according to its former and later shear rate value. Even so, this can also prove the validity of the proposed hypothesis, namely that the presence of slip boundary condition reduces the effective

shear rate within the system, therefore reducing the shear stress, which in turn provides the ability to reduce drag.

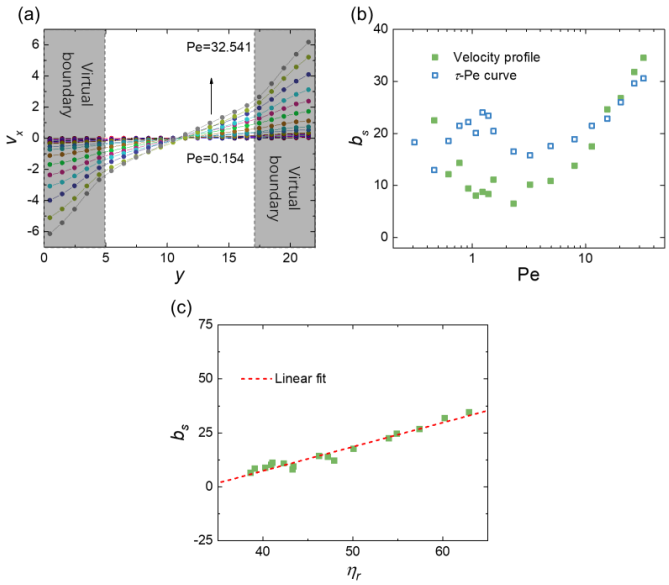

Figure 7. (a) The velocity profiles at Pe number ranged from 0.154 to 32.541 for partial slip boundary condition. (b) The slip length (b_s) varies against the Pe number, where the slip lengths are calculated using two methods, respectively. (c) The slip length (b_s) as a function of relative viscosity (η_r).

4. CONCLUSION

Based on the application of shear in confinement corresponding to Couette flow, a variety of boundary conditions, including no-slip and wall slip conditions, were employed to investigate the rheological properties and boundary layer behaviors of STFs to explore the link between fluid/wall interactions and non-Newtonian behaviors of the fluids. The experimental results show a different rheological behavior was obtained due to the decreased interaction of STFs to the substrate, which is associated with the lowered shear viscosity and delayed and diminished shear thickening. Therefore, a higher DR can be acquired by changing the boundary condition. Furthermore, based on the monotonic increase of shear stress versus shear rate, a non-standard method is proposed to estimate quantitatively slip length due to the change in

viscosity. The estimated slip length has a strong dependence on the shear rate which first decreases and subsequently increases with shear rate, contradicting the conventional knowledge of slip length variation for *e.g.* Newtonian fluids. We considered that this is related to the non-constant viscosity of STF under shearing. DPD simulations were adopted to corroborate the findings and computationally determine the slip length. The simulations' results are consistent with experimental results and provide a further justification of our findings. Furthermore, they confirm that slip length has a linear relationship with viscosity. By revealing this fundamental rheological phenomenon and the effect of amphiphobic substrates on boundary slip behavior of non-Newtonian fluids, this study provides new insights and will prove to be a useful reference for fluid dynamics research, industrial equipment and even for the development of impact protection solutions.

ASSOCIATED CONTENT

Supporting Information

The TEM image of SiO_2 Nanoparticles, the digital images of as-prepared STFs, the SEM images of morphology of as-prepared amphiphobic surface, the adhesive force of STFs to amphiphilic/amphiphobic substrates and the details of dissipative particle dynamic (DPD) simulation. (PDF)

AUTHOR INFORMATION

Corresponding Author

Wufang Yang,* E-mail: ywufang@licp.cas.cn. Tel: +86-931-4968177. Fax: +86-931-8277088

Feng Zhou,* E-mail: zhouf@licp.cas.cn. Tel: +86-931-4968466. Fax: +86-931-8277088.

Weimin Liu,* E-mail: wmliu@licp.cas.cn. Tel: +86-931-4968166. Fax: +86-931-

8277088.

Author contributions

Xingwei Wang, Wufang Yang and Jianbin Zhang conceived the idea, performed the experiments; Xingwei Wang, Wufang Yang and Jun Wen carried out the data curation and analyzation; Luyao Bao carried out the dispersive particle dynamic simulation; Xingwei Wang, Jun Wen, Luyao Bao and Wufang Yang wrote the original draft; Xingwei Wang, Daniele Dini, Wufang Yang, Feng Zhou and Weimin Liu reviewed the manuscript.

ACKNOWLEDGMENT

This work was financially supported by National Natural Science Foundation of China [grant numbers 21773274, 51905519] and Ministry of Science and Technology of China [2016YFC1100401]. D.D. acknowledges the support of the Engineering and Physical Sciences Research Council (EPSRC) via his Established Career Fellowship EP/N025954/1.

REFERENCES

(1) Han G, Nguyen T-B, Park S, Jung Y, Lee J, Lim H. Moth-Eye Mimicking Solid Slippery Glass Surface with Icephobicity, Transparency, and Self-Healing. ACS Nano 2020;14:10198-10209. https://doi.org/10.1021/acsnano.0c03463.

(2) Dong Z, Schumann MF, Hokkanen MJ, Chang B, Welle A, Zhou Q, et al. Superoleophobic Slippery Lubricant-Infused Surfaces: Combining Two Extremes in the Same Surface. Adv. Mater. 2018;30:1803890. https://doi.org/10.1002/adma.201803890.

(3) Tian C, Wang X, Liu Y, Yang W, Hu H, Pei X, et al. In Situ Grafting Hydrophilic Polymeric Layer for Stable Drag Reduction. Langmuir 2019;35:7205-7211. https://doi.org/10.1021/acs.langmuir.9b00321.

(4) Sun Q, Wang D, Li Y, Zhang J, Ye S, Cui J, et al. Surface charge printing for

programmed droplet transport. Nat. Mater. 2019;18:936-941. https://doi.org/10.1038/s41563-019-0440-2.

(5) Lu Y, Sathasivam S, Song J, Crick CR, Carmalt CJ, Parkin IP. Robust self-cleaning surfaces that function when exposed to either air or oil. Science 2015;347:1132-1135

(6) Lin Y, Shen Y, Liu A, Zhu Y, Liu S, Jiang H. Bio-inspiredly fabricating the hierarchical 3D porous structure superhydrophobic surfaces for corrosion prevention. Mater. Des. 2016;103:300-307. https://doi.org/10.1016/j.matdes.2016.04.083.

(7) Truesdell R, Mammoli A, Vorobieff P, Swol Fv, Brinker CJ. Drag reduction on a patterned superhydrophobic surface. Phys. Rev. Lett. 2006;97:044504. https://doi.org/10.1103/PhysRevLett.97.044504.

(8) Sasmal AK, Mondal C, Sinha AK, Gauri SS, Pal J, Aditya T, et al. Fabrication of superhydrophobic copper surface on various substrates for roll-off, self-cleaning, and water/oil separation. ACS Appl. Mater. Interfaces 2014;6:22034-43. https://doi.org/10.1021/am5072892.

(9) Rothstein JP. Slip on Superhydrophobic Surfaces. Annu. Rev. Fluid Mech. 2010;42:89-109. https://doi.org/10.1146/annurev-fluid-121108-145558.

(10) Choi W, Byeon H, Park JY, Kim IC, Lee SJ. Effects of pressure gradient on stability and drag reduction of superhydrophobic surfaces. Appl. Phys. Lett. 2019;114:101603. https://doi.org/10.1063/1.5085081.

(11) Voronov RS, Papavassiliou DV, Lee LL. Review of fluid slip over superhydrophobic surfaces and its dependence on the contact angle. Ind. Eng. Chem. Res. 2008;47:2455-2477

(12) Lee C, Kim C-J. Underwater restoration and retention of gases on superhydrophobic surfaces for drag reduction. Phys. Rev. Lett. 2011;106:014502. https://doi.org/10.1103/PhysRevLett.106.014502.

(13) Srinivasan S, Kleingartner JA, Gilbert JB, Cohen RE, Milne AJB, McKinley GH. Sustainable Drag Reduction in Turbulent Taylor-Couette Flows by Depositing Sprayable Superhydrophobic Surfaces. Phys. Rev. Lett. 2015;114:014501. https://doi.org/10.1103/PhysRevLett.114.014501.

(14) Jetly A, Vakarelski IU, Thoroddsen ST. Drag crisis moderation by thin air layers

sustained on superhydrophobic spheres falling in water. Soft Matter 2018;14:1608-1613. https://doi.org/10.1039/c7sm01904a.

(15) Haibao H, Peng D, Feng Z, Dong S, Yang W. Effect of hydrophobicity on turbulent boundary layer under water. Exp. Therm Fluid Sci. 2015;60:148-156. https://doi.org/https://doi.org/10.1016/j.expthermflusci.2014.08.013.

(16) Min T, Kim J. Effects of hydrophobic surface on skin-friction drag. Phys. Fluids 2004;16:L55-L58. https://doi.org/10.1063/1.1755723.

(17) Wen J, Reddyhoff T, Hu S, Puhan D, Dini D. Exploiting air cushion effects to optimise a superhydrophobic/hydrophilic patterned liquid ring sealed air bearing. Tribol. Int. 2020;144:106129. https://doi.org/https://doi.org/10.1016/j.triboint.2019.106129.

(18) Varshney P, Lomga J, Gupta PK, Mohapatra SS, Kumar A. Durable and regenerable superhydrophobic coatings for aluminium surfaces with excellent self-cleaning and anti-fogging properties. Tribol. Int. 2018;119:38-44. https://doi.org/https://doi.org/10.1016/j.triboint.2017.10.033.

(19) Kim SJ, Kim HN, Lee SJ, Sung HJ. A lubricant-infused slip surface for drag reduction. Phys. Fluids 2020;32:091901. https://doi.org/10.1063/5.0018460.

(20) Ybert C, Barentin C, Cottin-Bizonne C, Joseph P, Bocquet L. Achieving large slip with superhydrophobic surfaces: Scaling laws for generic geometries. Phys. Fluids 2007;19:123601. https://doi.org/10.1063/1.2815730.

(21) Yang W, Wu Y, Pei X, Zhou F, Xue Q. Contribution of Surface Chemistry to the Shear Thickening of Silica Nanoparticle Suspensions. Langmuir 2017;33:1037-1042. https://doi.org/10.1021/acs.langmuir.6b04060.

(22) Cao S, Pang H, Zhao C, Xuan S, Gong X. The CNT/PSt-EA/Kevlar composite with excellent ballistic performance. Compos. Pt. B-Eng. 2020;185:107793. https://doi.org/https://doi.org/10.1016/j.compositesb.2020.107793.

(23) Mawkhlieng U, Majumdar A. Deconstructing the role of shear thickening fluid in enhancing the impact resistance of high-performance fabrics. Compos. Pt. B-Eng. 2019;175:107167. https://doi.org/10.1016/j.compositesb.2019.107167.

(24) Galindo-Rosales FJ, Rubio-Hernández FJ, Sevilla A. An apparent viscosity

function for shear thickening fluids. J. Non-Newtonian Fluid Mech. 2011;166:321-325. https://doi.org/10.1016/j.jnnfm.2011.01.001.

(25) Sehgal P, Ramaswamy M, Cohen I, Kirby BJ. Using Acoustic Perturbations to Dynamically Tune Shear Thickening in Colloidal Suspensions. Phys. Rev. Lett. 2019;123:128001. https://doi.org/10.1103/PhysRevLett.123.128001.

(26) Cwalina CD, Wagner NJ. Rheology of non-Brownian particles suspended in concentrated colloidal dispersions at low particle Reynolds number. J. Rheol. 2016;60:47-59. https://doi.org/10.1122/1.4935445.

(27) Denn MM, Morris JF, Bonn D. Shear thickening in concentrated suspensions of smooth spheres in Newtonian suspending fluids. Soft Matter 2018;14:170-184. https://doi.org/10.1039/C7SM00761B.

(28) Hsu C-P, Ramakrishna SN, Zanini M, Spencer ND, Isa L. Roughness-dependent tribology effects on discontinuous shear thickening. Proc. Natl. Acad. Sci. U. S. A. 2018;115:5117-5122. https://doi.org/10.1073/pnas.1801066115.

(29) Lootens D, van Damme H, Hémar Y, Hébraud P. Dilatant Flow of Concentrated Suspensions of Rough Particles. Phys. Rev. Lett. 2005;95:268302. https://doi.org/10.1103/PhysRevLett.95.268302.

(30) James NM, Han E, de la Cruz RAL, Jureller J, Jaeger HM. Interparticle hydrogen bonding can elicit shear jamming in dense suspensions. Nat. Mater. 2018;17:965-970. https://doi.org/10.1038/s41563-018-0175-5.

(31) Brown E, Forman NA, Orellana CS, Zhang H, Maynor BW, Betts DE, et al. Generality of shear thickening in dense suspensions. Nat. Mater. 2010;9:220-224. https://doi.org/10.1038/nmat2627.

(32) Stöber W, Fink A, Bohn E. Controlled growth of monodisperse silica spheres in the micron size range. J. Colloid Interface Sci. 1968;26:62-69. https://doi.org/https://doi.org/10.1016/0021-9797(68)90272-5.

(33) Chen S-L, Dong P, Yang G-H. The Size Dependence of Growth Rate of Monodisperse Silica Particles from Tetraalkoxysilane. J. Colloid Interface Sci. 1997;189:268-272. https://doi.org/https://doi.org/10.1006/jcis.1997.4809.

(34) Wu W, Wang X, Wang D, Chen M, Zhou F, Liu W, et al. Alumina nanowire forests

via unconventional anodization and super-repellency plus low adhesion to diverse liquids. Chem. Commun. 2009:1043-1045. https://doi.org/10.1039/B818633B.

(35) Cheng X, McCoy JH, Israelachvili JN, Cohen I. Imaging the microscopic structure of shear thinning and thickening colloidal suspensions. Science 2011;333:1276-1279

(36) Wagner NJ, Brady JF. Shear thickening in colloidal dispersions. Phys. Today 2009;62:27-32

(37) Boersma WH, Laven J, Stein HN. Computer simulations of shear thickening of concentrated dispersions. J. Rheol. 1995;39:841-860. https://doi.org/10.1122/1.550621.

(38) Lin NY, Guy BM, Hermes M, Ness C, Sun J, Poon WC, et al. Hydrodynamic and Contact Contributions to Continuous Shear Thickening in Colloidal Suspensions. Phys. Rev. Lett. 2015;115:228304. https://doi.org/10.1103/PhysRevLett.115.228304.

(39) Xue Y, Wu Y, Pei X, Duan H, Xue Q, Zhou F. How Solid–Liquid Adhesive Property Regulates Liquid Slippage on Solid Surfaces? Langmuir 2015;31:226-232. https://doi.org/10.1021/la503972m.

(40) Cheng M, Song M, Dong H, Shi F. Surface Adhesive Forces: A Metric Describing the Drag-Reducing Effects of Superhydrophobic Coatings. Small 2015;11:1665-1671. https://doi.org/10.1002/smll.201402618.

(41) Jamali S, Brady JF. Alternative Frictional Model for Discontinuous Shear Thickening of Dense Suspensions: Hydrodynamics. Phys. Rev. Lett. 2019;123:138002. https://doi.org/10.1103/PhysRevLett.123.138002.

(42) Smiatek J, Allen MP, Schmid F. Tunable-slip boundaries for coarse-grained simulations of fluid flow. Eur. Phys. J. E 2008;26:115-22. https://doi.org/10.1140/epje/i2007-10311-4.

(43) Guo L, Wong PL, Guo F. Effects of viscosity and sliding speed on boundary slippage in thin film hydrodynamic lubrication. Tribol. Int. 2017;107:85-93. https://doi.org/https://doi.org/10.1016/j.triboint.2016.11.021.

Captions of figure:

Figure 1. Schematic illustration of the Couette flows of STFs with no-slip and slip boundary conditions and the definition of slip lengths b_s.

Figure 2. Viscosity curves as functions of shear rate for STFs with increasing NPs volume fractions.

Figure 3. Flow curves and viscosity curves of STFs with NPs volume fraction being (a) 36.5% and (b) 45.5% under no-slip and slip boundary conditions and their corresponding drag reductions.

Figure 4. Two kinds of shear rate illustrated on the flow curves of STFs.

Figure 5. The total slip length as a function of shear rate for STFs with NPs volume fractions being (a) 36.5% and (b) 45.5%, respectively.

Figure 6. The rheology of model STFs under slip and no-slip boundary conditions and its corresponding drag reduction.

Figure 7. (a) The velocity profiles at Pe number ranged from 0.154 to 32.541 for partial slip boundary condition. (b) The slip length (b_s) varies against the Pe number, where the slip lengths are calculated using two methods, respectively. (c) The slip length (b_s) as a function of relative viscosity (η_r).

Figures:

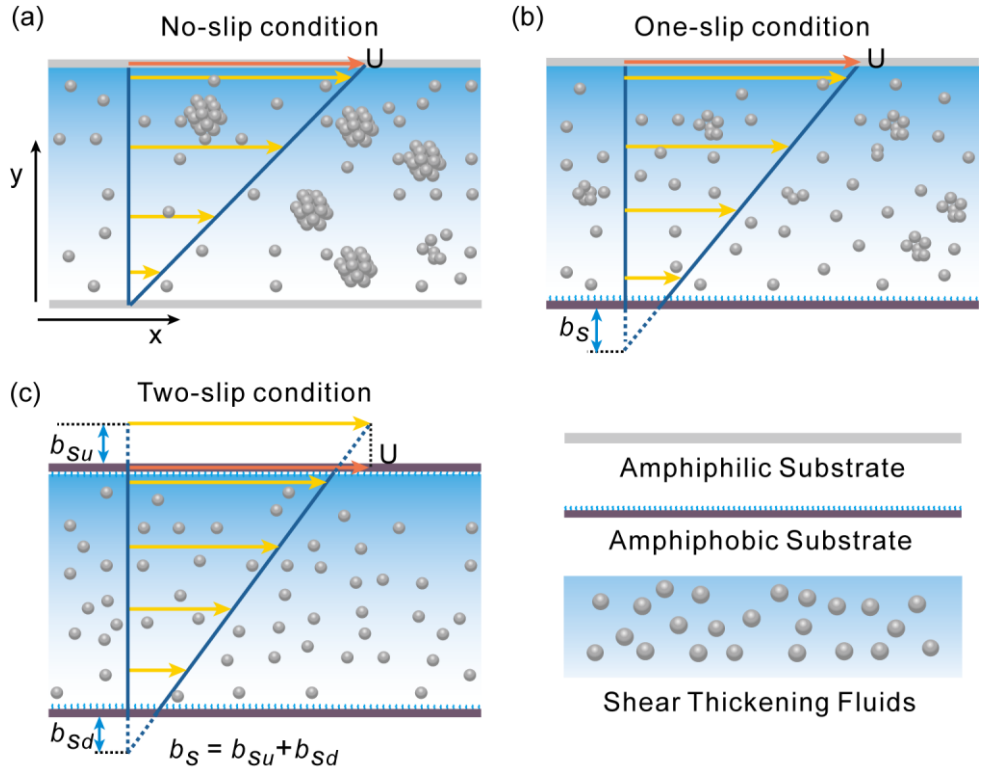

Figure 1

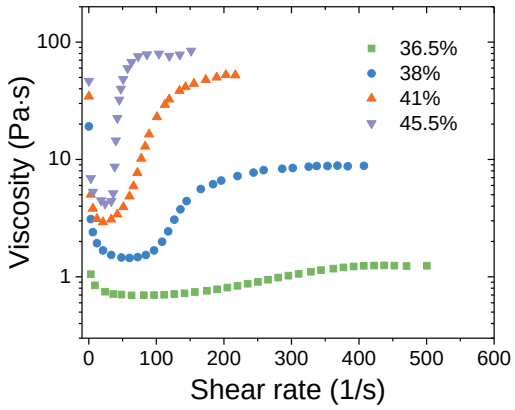

Figure 2

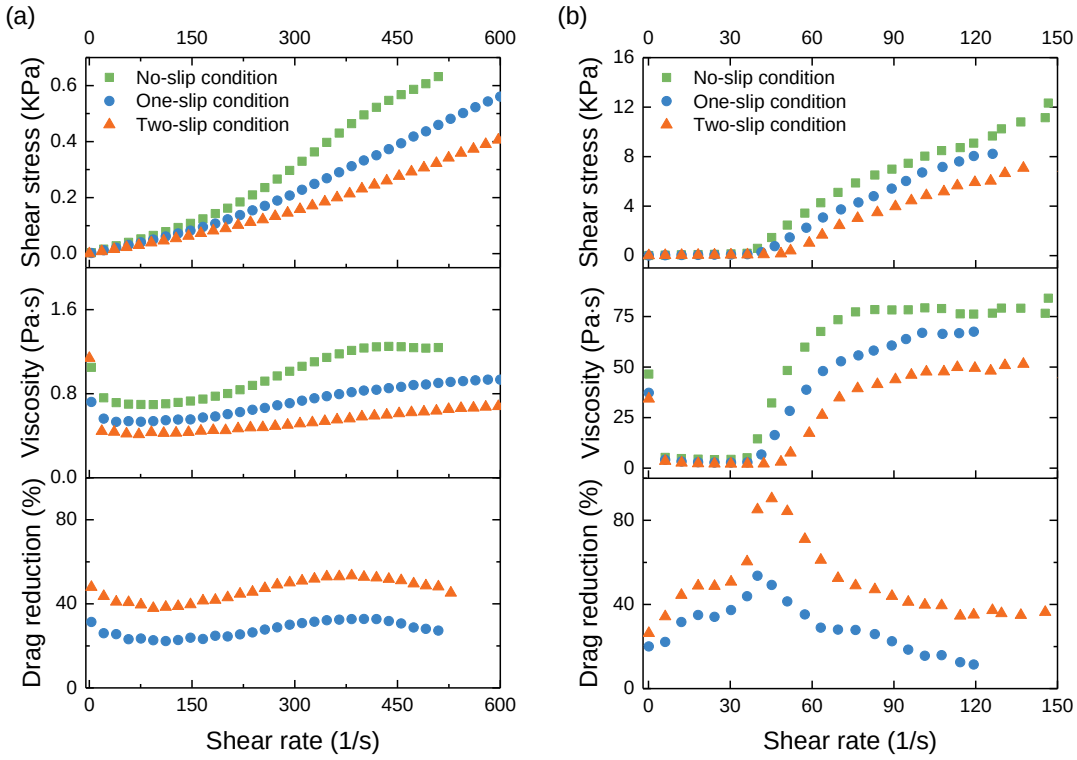

Figure 3

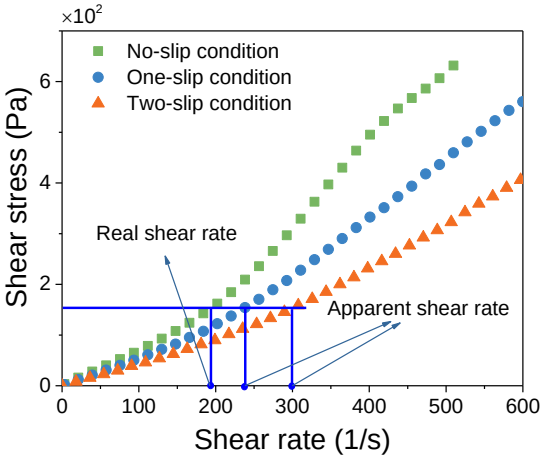

Figure 4

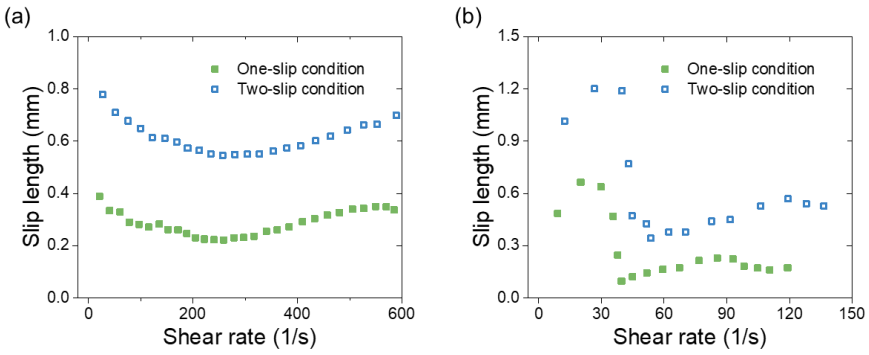

Figure 5

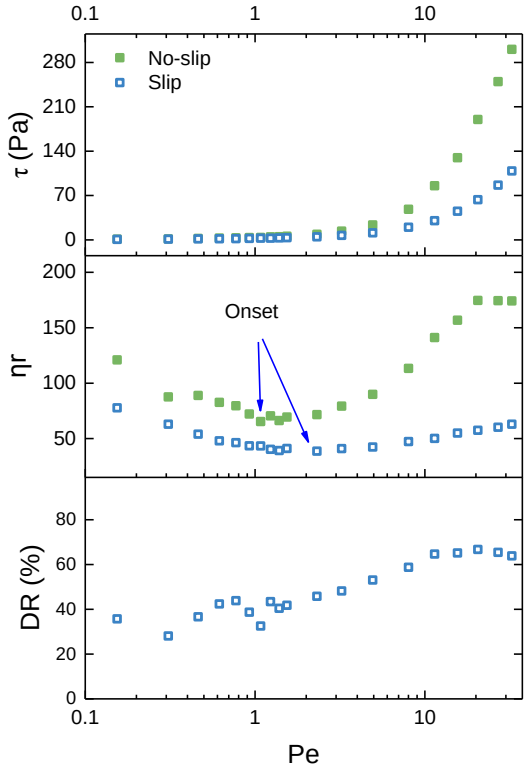

Figure 6

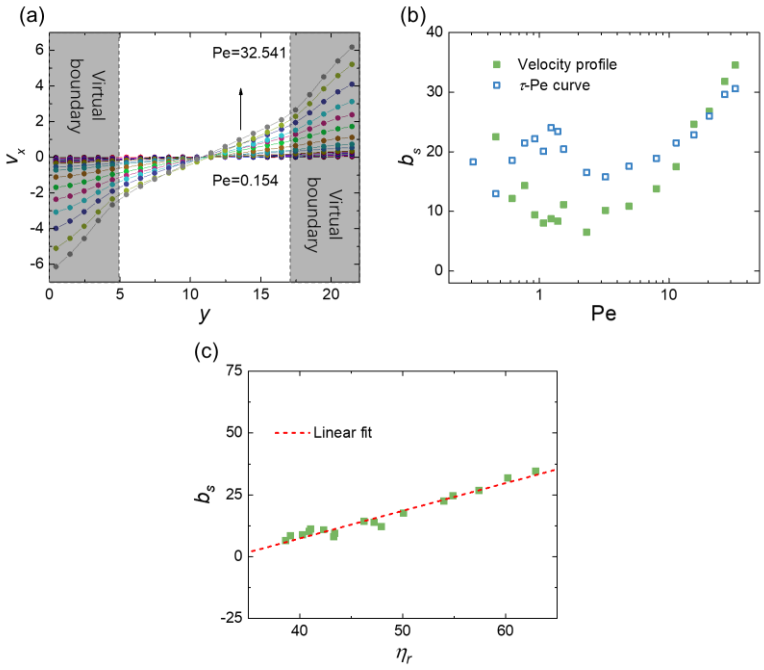
(a)
Virtual boundary
Pe=32.541
Pe=0.154
Virtual boundary
v_x
y
(b)
Velocity profile
τ-Pe curve
b_s
Pe
(c)
Linear fit
b_s
η_r

Figure 7

Captions of table:

Table 1. Critical shear rates of STFs with different NPs volume fraction upon Couette flow under distinct boundary conditions and their corresponding critical shear rate hysteresis.

Table:

Table 1

Mass fraction	$\dot{\gamma}_c$/s^{-1}			$\Delta\dot{\gamma}_c$/s^{-1}	
	No-slip condition	One-slip condition	Two-slip condition	One-slip condition	Two-slip condition
45.5%	36.9	40.8	51.3	3.9	14.4
36.5%	160.8	172.3	195.4	11.5	34.6